Supporting Information

Experimental section

Preparation of $(NH_4)_2Co_8(CO_3)_6(OH)_6 \cdot 4H_2O$ nanosheet precursors: For the synthesis of nanosheet precursors, a mixed solution of ethylene glycol (12.5 mL), $NH_3 \cdot H_2O$ (12.5 mL), Na_2CO_3 solution (1 M, 5 mL) and $Co(NO_3)_2$ solution (1 M, 5 mL) was poured into a Teflon-lined liner and a temperature-rise period was further exerted at 170 ^oC for 17 h. With the termination of reaction process, the precursors were collected and rinsed by ultrapure water and ethyl alcohol when the temperature was cooled down indoor temperature. Finally, the samples were dried at 60 ^oC for subsequent use.

Preparation of sandwich-like Co nanoparticles composites intermediates: For subsequent preparation, 100 mg the nanosheet precursors were soaked in 25mL 0.2 M glucose solution and then they were ultrasonically mixed for 5 min. Following that, the above solution was diverted into the Teflon-lined liner and heated up to 180 ^oC for 8h. After that, the nanosheet precursors wrapped with a layer of polymer on the surface were obtained. Afterwards, the above intermediates were placed in graphite boat and burned at 720 ^oC under H_2 atmosphere for 200 min to gain the sandwich-like Co nanoparticles composites.

Preparation of sandwich-like $CoTe_{2x}Se_{2(1-x)}$ composites: The selenization and telluridization reactions were simultaneously conducted in the temperature programmed process. In brief, 100 mg the sandwich-like Co composite was put in the downstream part of the graphite boat with a cover, while 1 g mixture of tellurium and selenium powders with various ratios was placed at the upstream position. Then, the graphite boat with a cover on it was put in a horizontal quartz tube furnace. Following that, a drastic heating process was performed in the quartz tube furnace at Ar atmosphere from 20 ^oC to 700 ^oC with a rate of 10 ^oC min^{-1}. During this process, sandwich-like Co nanoparticles were successfully transformed into sandwich-like $CoTe_{2x}Se_{2(1-x)}$ composites.

Preparation of sandwich-like $CoS_{2y}Se_{2(1-y)}$ composites: For the preparation of sandwich-like $CoS_{2y}Se_{2(1-y)}$ composites, except for the different calcinations temperature, the experimental procedures followed the same processes as those of sandwich-like $CoTe_{2x}Se_{2(1-x)}$ composites by altering the tellurium powders to sulfur powders.

Preparation of sandwich-like $CoSe_2$ composites: For comparison, sandwich-like $CoSe_2$ composite was also prepared. In the second burning process, the individual selenium powder replaced the mixed powders of tellurium and selenium powders. Other experimental procedures are same as those of sandwich-like $CoTe_{2x}Se_{2(1-x)}$ composite.

Preparation of $CoSe_2$ bulks: Compared with fabricating sandwich-like $CoTe_{2x}Se_{2(1-x)}$ composites, the experimental steps omitted the hydrothermal process of coating glucose polymer. Likewise, the individual selenium powder substituted the mixed powders of tellurium and selenium powders. Other experimental steps are similar to these of sandwich-like $CoTe_{2x}Se_{2(1-x)}$ composite.

The detailed experimental conditions for above samples were also listed in Table S10.

Characterization: The powder X-ray diffractometer (Bruker D8 Advance, Cu Kα radiation (λ = 1.54184 Å)), Raman spectrometer equipped with argon (532 nm) laser in the wavenumber of 100-2000 cm^{-1} (Horiba LabRAM HR Evolution) and X-ray photoelectron spectrometer (ESCALAB250), Brunauer-Emmett-Teller surface area analyzer (BET, Quantachrome Autosorb-6B), Scanning Electron Microscope (JEOL JSM-7800F) and Transmission Electron Microsphere (Philips, Tecnai, F30) were carried out to test the pure phase, component, valence states, surface

area, morphology and structural features of as-prepared samples.

Electrochemical characterization: For the preparation of working electrode, the as-obtained samples were dispersed a liquid mixture with 10% Nafion (0.5 wt%) and 90% ethanol to form well-proportioned slurry. Then the slurry was uniformly overlaid on Ni foam with a cover area of 1 cm^2 as working electrode. The loading mass of tested samples was controlled at 1± 0.1 mg cm^{-2} as much as possible. The electrochemical performance was researched using an electrochemical station (CHI660D, shanghai) in a common tree-electrode setup with 1 M KOH electrolyte. Meanwhile, saturated calomel electrode (SCE) and graphite plate were used as reference and counter electrode, respectively. And all the voltage values were expressed by the reversible hydrogen electrode (RHE), in the light of the Nernst equation: $E_{(RHE)} = E_{(SCE)} + 0.0592\ pH + 0.241$.

Before recording the test results, the cyclic voltammetry (CV) was firstly measured for at least 10 cycles for the purpose of achieving the stable state. The linear sweep voltammetry (LSV) was performed at 3 mV s^{-1} to gain the polarization profiles and Tafel slopes. The voltage scope of OER and HER measurement is 0-0.6 V and -1.6-1 V, respectively. The stability evaluation of OER and HER was conducted by chronopotentiometric measurements at 10 mA cm^{-2} and -10 mA cm^{-2}, respectively. Electrochemical impedance spectroscopy (EIS) was applied in the frequency region of 10^5-10^{-2} Hz in potentiostatic mode. And the Zview version 3.2c-software was used to parse the impedance data for OER and HER. The full water splitting was conducted in a two-electrode system with 1 M KOH electrolyte at 3 mV/s, and as-prepared samples were used as anode and cathode, respectively.

Carbon content: The as-synthesized sandwich-like samples (500 mg) were soaked in 100 mL 8 M HNO_3 aqueous solution, accompanying with continuous stirring for at least 50 h. Until the active nanoparticles were absolutely dissolved, the residual graphitized carbon was collected, washed and dried. Then, an analytical balance was used to weight the mass of the as-obtained graphitized carbon. Afterwards, the following computational formula was applied to compute carbon content of as-gained samples.

$$C\%=W(C)/W(\text{sandwich-like samples})\times 100\%$$

Wherein, W(C) and W (sandwich-like samples) stood for the mass of graphitized carbon and sandwich-like samples, respectively. The results revealed that the carbon contents in those sandwich-like samples ($CoTe_{2x}Se_{2(1-x)}$ and $CoS_{2y}Se_{2(1-y)}$) mainly drop into the scope of 6.8-7.2 Wt.%.

Theoretical calculation

Computation details

All the computations were performed by using the generalized gradient approximation (GGA) with the Perdew-Burke-Ernzerh (PBE)[1] within the DFT framework as implemented in Vienna *ab initio* simulation package (VASP).[2] The wave functions were expanded in a plane wave basis truncated at a plane wave energy of 500eV, and a 4×4×4 Monkhorst-Pack grid was used for ƙ-space sampling in the calculation.[3] For the geometry optimizations, the force and energy cutoff were set as 0.03eV/Å and 10^{-5}eV. A vacuum space as large as 15 Å was used along the c direction normal to the catalyst surface to avoid periodic interactions. The $Co(S_{0.31}Se_{0.69})_2$, $Co(S_{0.45}Se_{0.55})$, $Co(S_{0.62}Se_{0.38})_2$, $Co(S_{0.72}Se_{0.28})_2$ and CoS_2 crystal structures were built by substituting S with Se in $CoSe_2$ crystal structure, respectively. The bottom three layers were fixed, all the other atoms were fully relaxed.[4]

Calculations of the Hydrogen Evolution Reaction

It is well known that the Hydrogen Evolution Reaction (HER) activity over a give system can be closely correlated to the adsorption energy of a single H atom on the system. Thus, the free energy of H^*(ΔG(H^*)) is usually considered as an effective descriptor for evaluating HER activity on the system, where in general, the smaller $\Delta G(H*)$ absolute value, the better the HER activity over the system.[5] The free energy of adsorbed state was calculated as:

$$\Delta G(H*) = \Delta E(H*) + \Delta ZPE - T\Delta S$$

Where $\Delta E(H*)$ is the hydrogen chemisorption energy, ΔZPE is the zero point energy difference between adsorbed and the gas phase and $T\Delta S$ is the entropy change of H*. ΔS was calculated by the formula:

$$\Delta S = S(H*) - \frac{1}{2}S(H_2) \approx -\frac{1}{2}S(H_2)$$

Where $S(H_2)$ is the entropy of H_2 in the gas phase at standard condition. Considering that TS(H_2) is 0.4 eV for H_2 at 298K and 1 atm, the corresponding TΔS was determined to be -0.20 eV. Furthermore, the equation $\Delta ZPE = ZPE(H*)$ was employed to estimate zero point energy change of H*. Our computed value of ZPE (H_2) was 0.277 eV, which is close to the value of Nørskov et al.[6]

As is shown in the Table S5, we calculate that the values of $\Delta E(H*)$, $ZPE(H*)$,ΔZPE and $\Delta G(H*)$ of the H* at the different adsorption of different models. It's evident that the hydrogen atom adsorbed at Co site of $Co(S_{0.72}Se_{0.28})_2$ has the smallest Gibbs free energy up to 0.183 eV, which proves the best HER activity. Of course, the result of the calculation also shows that the relative HER activity is in the order of $Co(S_{0.72}Se_{0.28})_2$ > $Co(S_{0.45}Se_{0.55})_2$ > $Co(S_{0.31}Se_{0.69})_2$ >$CoSe_2$ > CoS_2, which is well agreement with our experimental results.

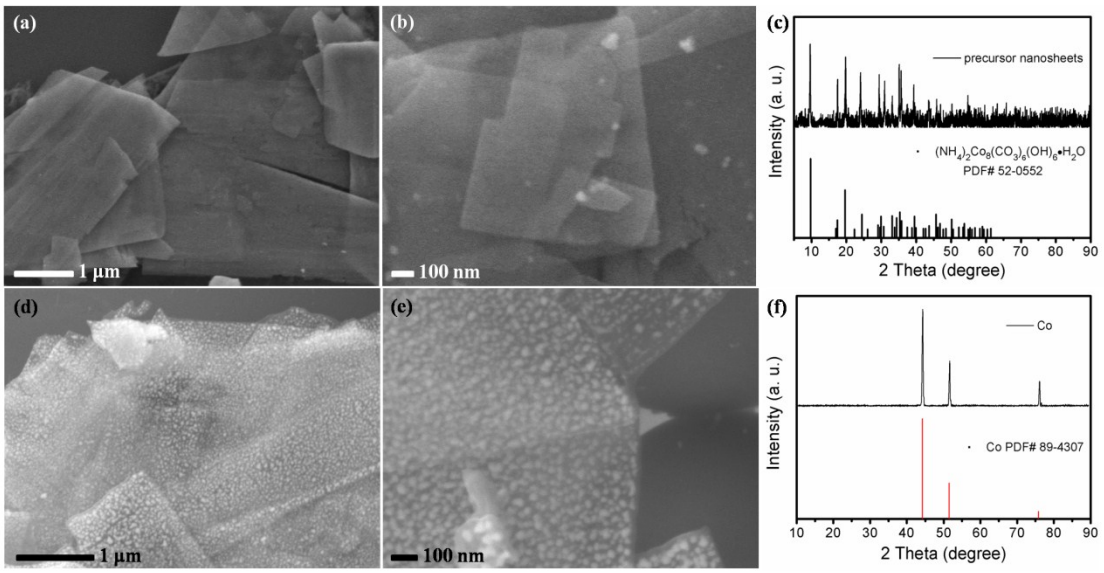

Figure S1. (a) The low-resolution SEM image, (b) the high-resolution SEM image and (c) the XRD pattern of $(NH_4)_2Co_8(CO_3)_6(OH)_6 \cdot H_2O$ nanosheet precursors. (d) The low-resolution SEM image, (e) the high-resolution SEM image and (f) the XRD pattern of the sandwich-like Co nanoparticle intermediates.

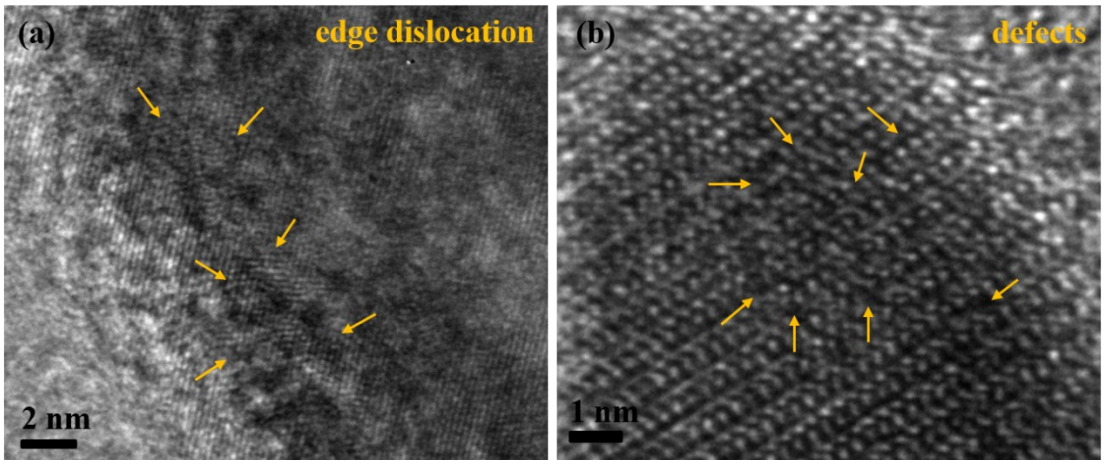

Figure S2. (a) the HRTEM image of individual $Co(Te_{0.33}Se_{0.67})_2$ nanoparticle to confirm the edge dislocation, and (b) the enlarged HRTEM image to display the defects caused by the Te-doping.

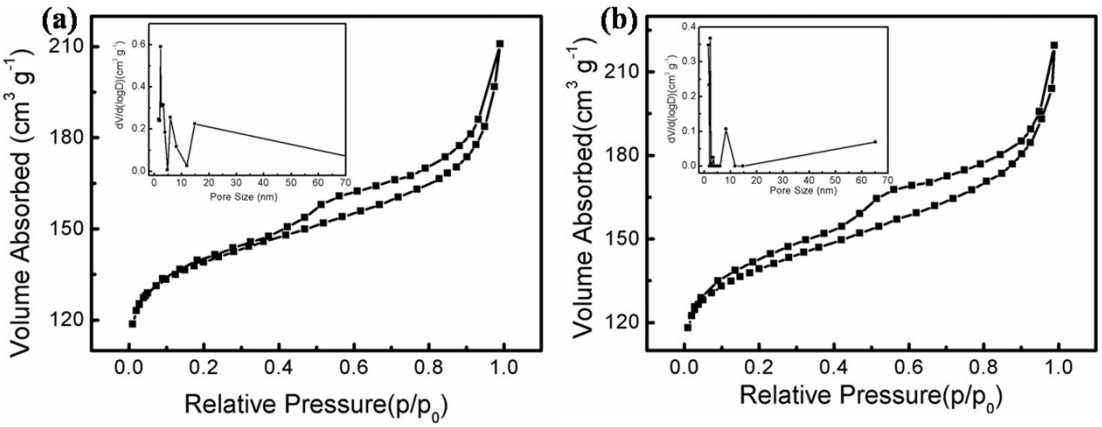

Figure S3. Nitrogen adsorption-desorption isotherm and the corresponding pore size distribution (inset) of (a) sandwich-like $Co(Te_{0.33}Se_{0.67})_2$ graphitized carbon-based composite and (b) sandwich-like $Co(S_{0.72}Se_{0.28})_2$ graphitized carbon-based composite.

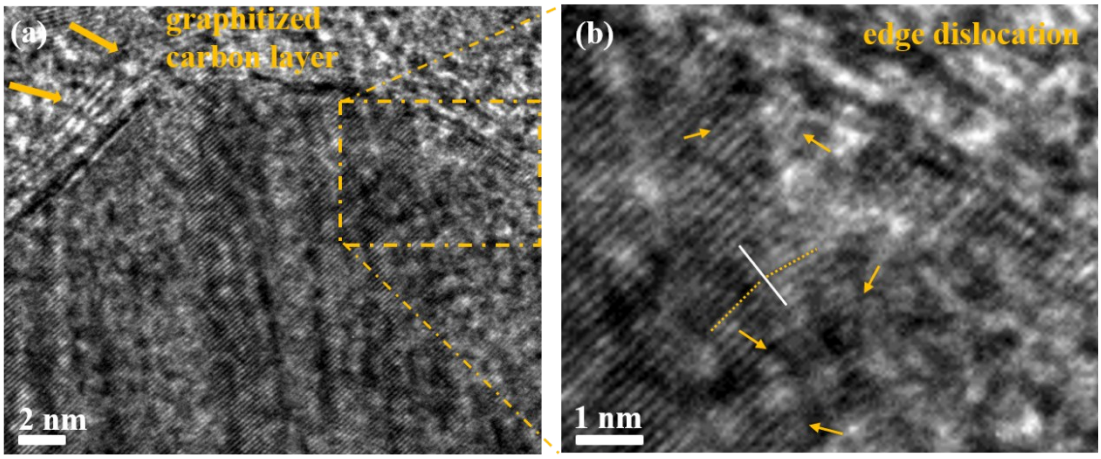

Figure S4 (a) the HRTEM image of individual $Co(S_{0.72}Se_{0.28})_2$ nanoparticle and (b) the enlarged HRTEM image taken from yellow dashed box of Figure S4a.

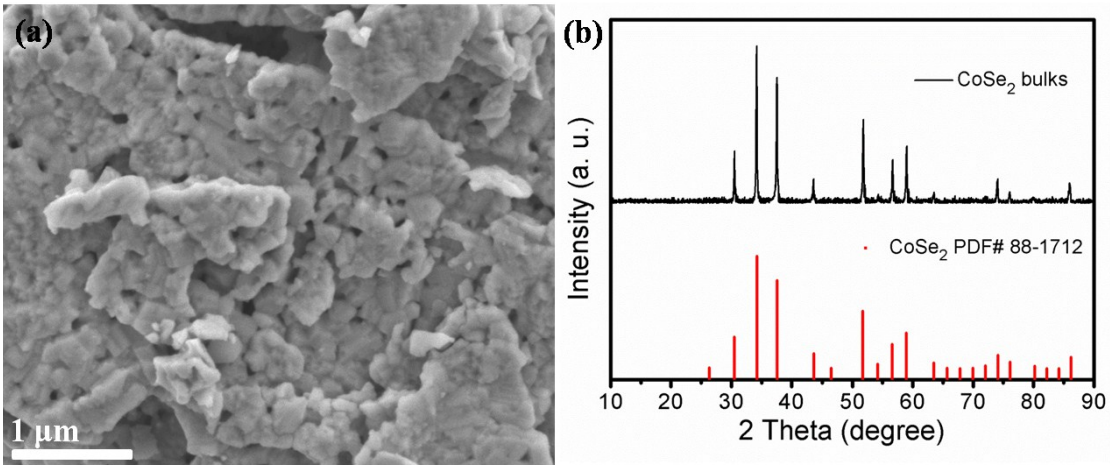

Figure S5. The SEM image and XRD pattern of $CoSe_2$ bulks.

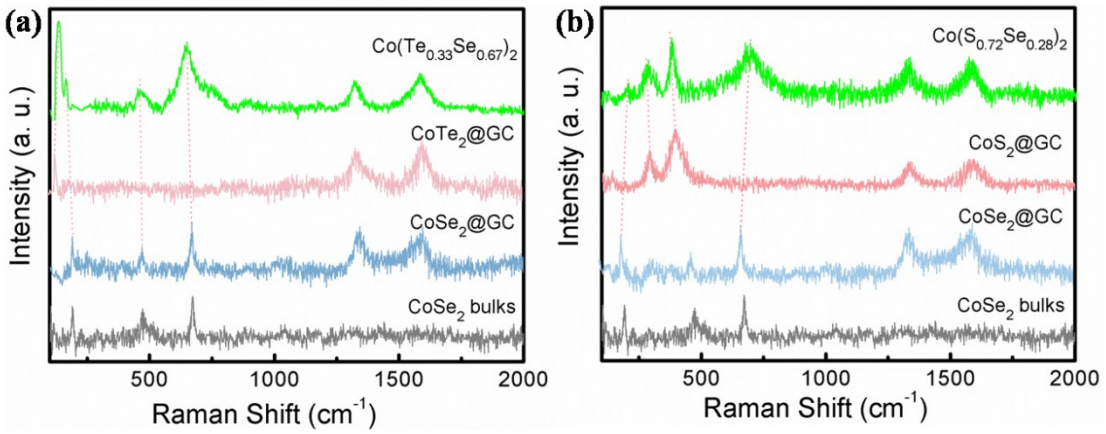

Figure S6. (a) Raman spectra of sandwich-like $Co(Te_{0.33}Se_{0.67})_2$, $CoTe_2$@GC, $CoSe_2$@GC and $CoSe_2$ bulks. (b) Raman spectra of sandwich-like $Co(S_{0.72}Se_{0.28})_2$, CoS_2@GC, $CoSe_2$@GC and $CoSe_2$ bulks.

Further insights into the electronic structures of as-obtained samples were acquired from Raman spectroscopy, which is also a crucial means to characterize the structure and quality of carbonaceous materials.[7] To highlight the advantages of component and morphology, we also synthesized the sandwich-like $CoTe_2$ (labeled as $CoTe_2$@GC), sandwich-like CoS_2 (CoS_2@GC), sandwich-like $CoSe_2$ ($CoSe_2$@GC) and $CoSe_2$ bulks, and compared with their Raman spectra in Figure S6. The Raman spectra of $CoSe_2$@GC and $CoSe_2$ bulks display three characteristic modes at 190, 474 and 671 cm^{-1}, consistent with the reported values of $CoSe_2$.[8] An obvious peak at 120 cm^{-1} is detected in the Raman spectrum of $CoTe_2$@GC, indexing to the intense Te-Te stretch mode (Figure S6a).[9] Additionally, two Raman modes (A_g at 396 cm^{-1} and E_g at 290 cm^{-1}) are also appeared in the Raman spectrum of CoS_2@GC (Figure S6b), wherein the A_g and E_g represent the in-phase stretching vibration and librational vibration of sulfur atoms in the dumbbells, respectively. Notably, there are two groups of constituent-dependent modes in the Raman spectra of both sandwich-like $Co(Te_{0.33}Se_{0.67})_2$ and $Co(S_{0.72}Se_{0.28})_2$ composites. For sandwich-like $Co(Te_{0.33}Se_{0.67})_2$, one located at the low wave number of 100-150 cm^{-1} is associated with the Co-Te vibration mode, the other settled in the high wave number of 400-800 cm^{-2} is related to the Co-Se vibration mode (Figure S6a). And sandwich-like $Co(S_{0.72}Se_{0.28})_2$ also owns two sets of constituent-dependent vibration modes: Co-S mode and Co-Se mode at 250-450 cm^{-1} and 550-850 cm^{-1}, respectively. Such two-mode behavior is the typical symbol of the solid solution phase, similar to the literatures.[10] More importantly, due to the possible changes in bond polarization, the introduction of Te atoms and S atoms changes chemical environment of Co-Se mode, resulting in the slight shift of vibration modes (the similar phenomena are also discovered in Se doped MoS_2 [11] and P doped CoS_2[12]).

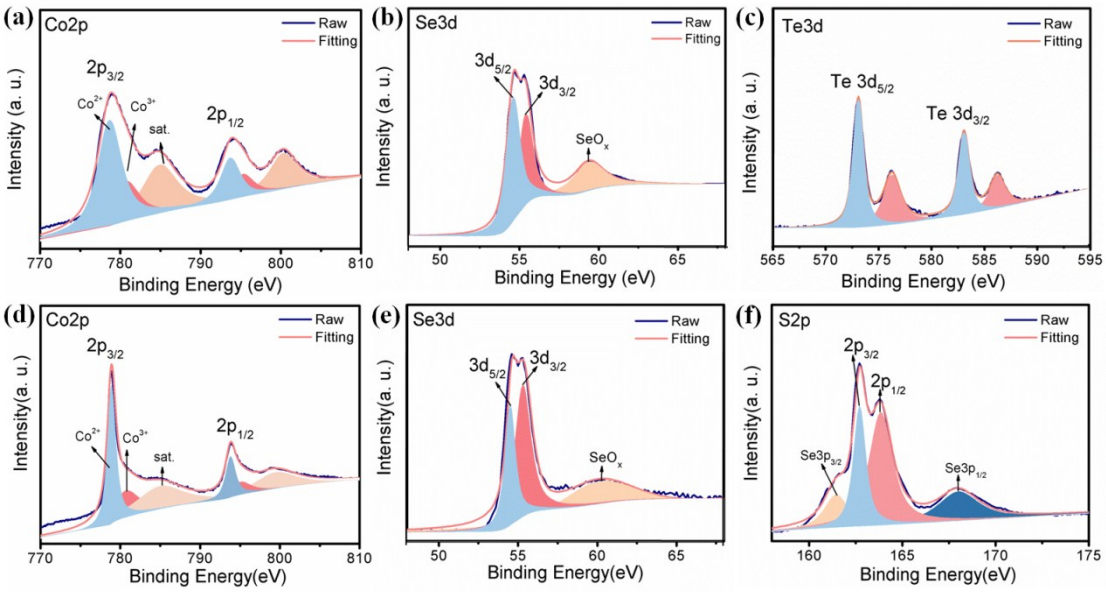

Figure S7. XPS spectra of (a) Co 2p, (b) Se 3d and (c) Te 3d in sandwich-like $Co(Te_{0.33}Se_{0.67})_2$ composite. XPS spectra of (d) Co 2p, (e) Se 3d and (f) S 2p in sandwich-like $Co(S_{0.72}Se_{0.28})_2$ composite.

It's widely reported that the catalytic activity of electrocatalysts has an affinity with the valence states and coordinated environment of central metal ions.[13] Especially for TMDs, the divalent metal cations with low-spin states are octahedrally bonded with chalcogen dimers. Thus, X-ray photoelectron spectroscopy (XPS) was adopted to characterize the surface chemical composition and elemental bonding configuration. Figure S7a-c reveal the XPS spectra of the sandwich-like $Co(Te_{0.33}Se_{0.67})_2$. In the Co 2p region (Figure S7a), two principal peaks are situated at 778.8 eV and 793.8 eV, corresponding to the Co $2p_{3/2}$ and Co $2p_{1/2}$ signals, respectively. Apparently, the two peaks are asymmetrical, thus they are split into four sub-peaks. The dominant peaks at 778.9 eV and 793.9 eV are assigned to the Co^{2+} ions.[14] The electron-binding energies of $Co2p_{3/2}$ at 780.8 eV and $Co2p_{1/2}$ at 795.3 eV are indexed to the Co-O bonding of amorphous oxide layers on the surface.[15, 16] Additionally, two satellite peaks at the side of Co2p signal are observed, which manifests the antibonding orbital between chalcogen atoms and cobalt atoms.[17] Owing to the ligand effects and oxidation states, the XPS peaks of Co2p exhibit multiple splitting and satellites. In the Co-based TMDs, the first coordination shell of Co atom is distorted octahedron with six covalently bonded chalcogen atoms. Thus, the d-electron configuration of cobalt cations immensely affects their physicochemical properties. According to the crystal filed theory, the 3d bands of transition metal atoms are split into bonding orbits (t_{2g}) and antibonding orbits (e_g). In terms of the electron configuration of Co 3d bands, six 3d electrons fully occupy the t_{2g} orbits and one electron fills the e_g orbits to form the low-spin ground state of $t_{2g}^6 e_g^1$. Therefore, the charge transferred from the ligands can only occupy the antibonding e_g orbits, indicating the metallic character.[18] The metallic properties allow the valid migration of electrons from the surface to the inner to contribute the highly electrocatalytic performance. Figure S7b displays the high-resolution XPS spectrum of Se3d.The major peak is fitted into two sub-peaks at bonding energies of 54.5 eV and 55.3 eV, corresponding to the $Se3d_{5/2}$ and $Se3d_{3/2}$ signals, respectively, which is

ascribed to the metal-selenium bond.[15] The broad peak near 60 eV is indexed to the Se-O bond, implying the surface oxidation of Se species.[19] Besides, Te3d core level XPS spectrum (Figure S7c) exhibits that Te $3d_{5/2}$ and Te $3d_{3/2}$ peaks are positioned at 573.1 and 583.0 eV, respectively, in well conformity with the values in literatures, implying the distinctive Te_2^{2-} signals in the Te 3d region.[9] And the satellite peaks at 576.2 and 586.3 eV suggest the oxidation of Te on the surface.[20] Likewise, Figure S7d-f display the XPS spectra of sandwich-like $Co(S_{0.72}Se_{0.28})_2$. The Co2p and Se3d spectra of $Co(S_{0.72}Se_{0.28})_2$ present the similar behaviors to those of $Co(Te_{0.33}Se_{0.67})_2$. Notably, the S2p XPS spectrum is deconvoluted into four peaks. The dominant peaks are located at 162.7 eV and 163.8 eV, referring to $S2p_{3/2}$ and $S2p_{1/2}$, respectively, implying the existence of pyrite lattice sulfide.[21].

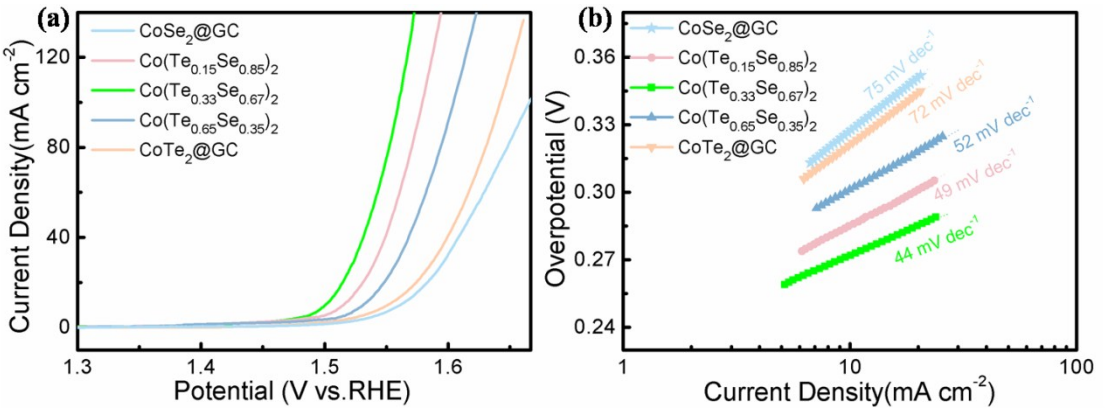

Figure S8. (a) OER polarization curves and (b) OER Tafel slopes of sandwich-like $CoSe_2$, $Co(Te_{0.15}Se_{0.85})_2$, $Co(Te_{0.33}Se_{0.67})_2$, $Co(Te_{0.65}Se_{0.35})_2$ and $CoTe_2$ graphitized carbon-based composites.

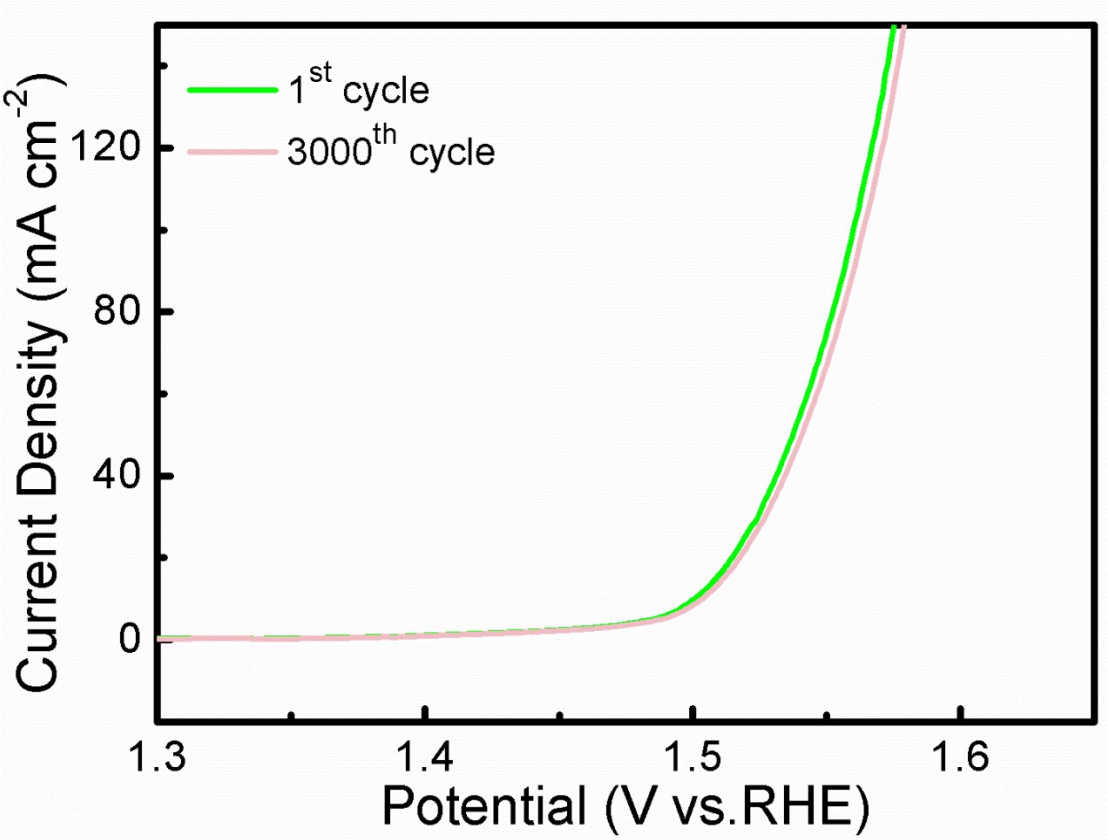

Figure S9. OER LSV curves of sandwich-like $Co(Te_{0.33}Se_{0.67})_2$ graphitized carbon-based composite for 1st and 3000th cycles at a scan rate of 3 mV s^{-1} in 1M KOH electrolyte.

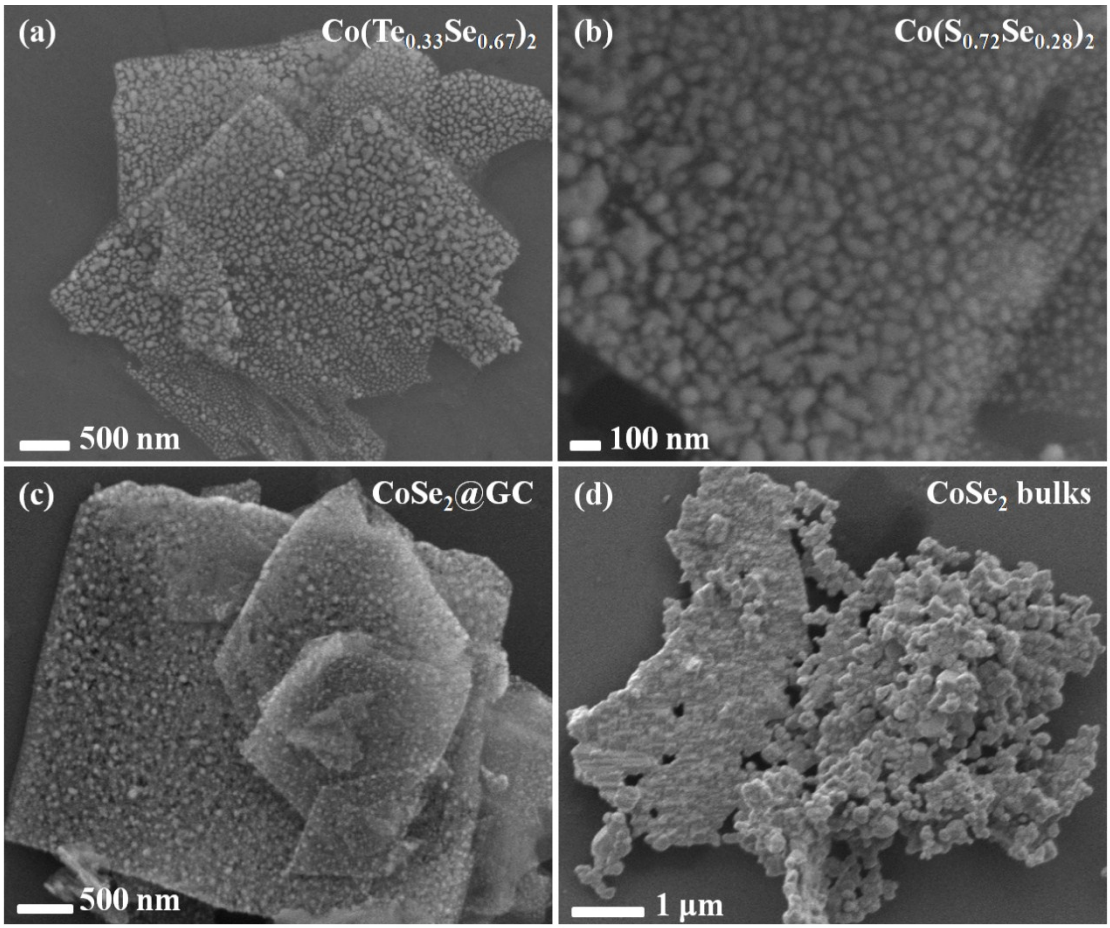

Figure S10. The SEM images of (a) sandwich-like $Co(Te_{0.33}Se_{0.67})_2$, (b) $Co(S_{0.72}Se_{0.28})_2$, (c) $CoSe_2$@GC and (d) $CoSe_2$ bulks after OER measurements.

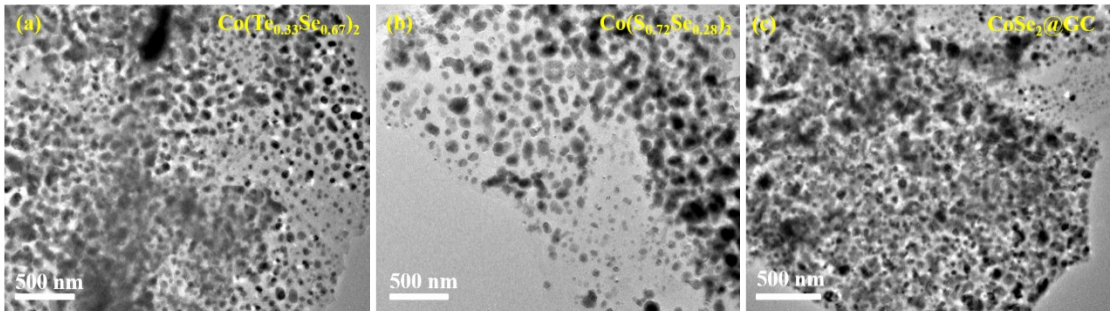

Figure S11. The TEM images of (a) sandwich-like $Co(Te_{0.33}Se_{0.67})_2$, (b) $Co(S_{0.72}Se_{0.28})_2$ and (c) $CoSe_2$@GC after OER measurements.

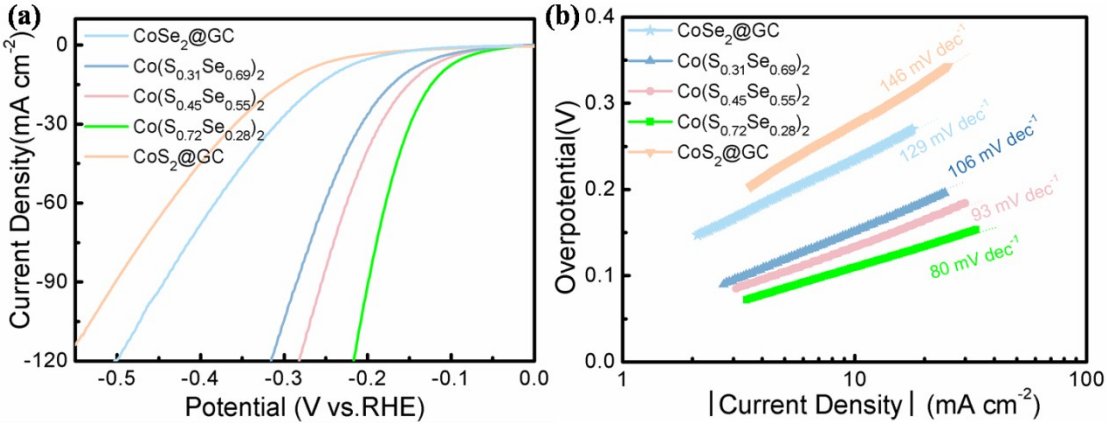

Figure S12. (a) HER polarization curves and (b) HER Tafel slopes of sandwich-like $CoSe_2$, $Co(S_{0.31}Se_{0.69})_2$, $Co(S_{0.45}Se_{0.55})_2$, $Co(S_{0.72}Se_{0.28})_2$ and CoS_2 graphitized carbon-based composites.

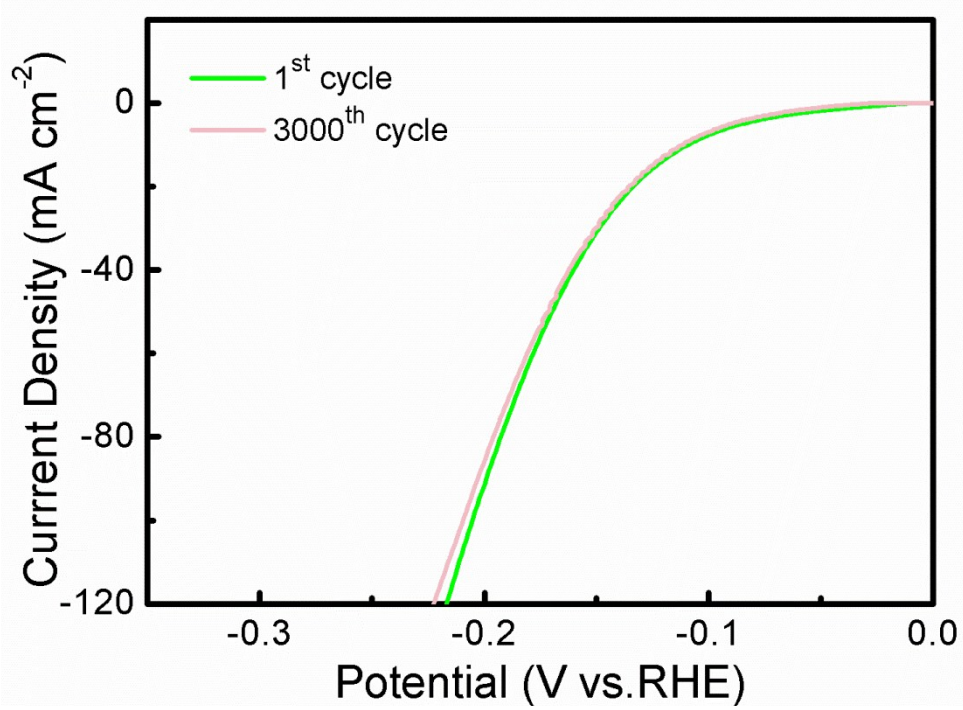

Figure S13. HER LSV curves of sandwich-like $Co(S_{0.72}Se_{0.28})_2$ graphitized carbon-based composite for 1st and 3000th cycles at a scan rate of 3 mV s^{-1} in 1M KOH electrolyte.

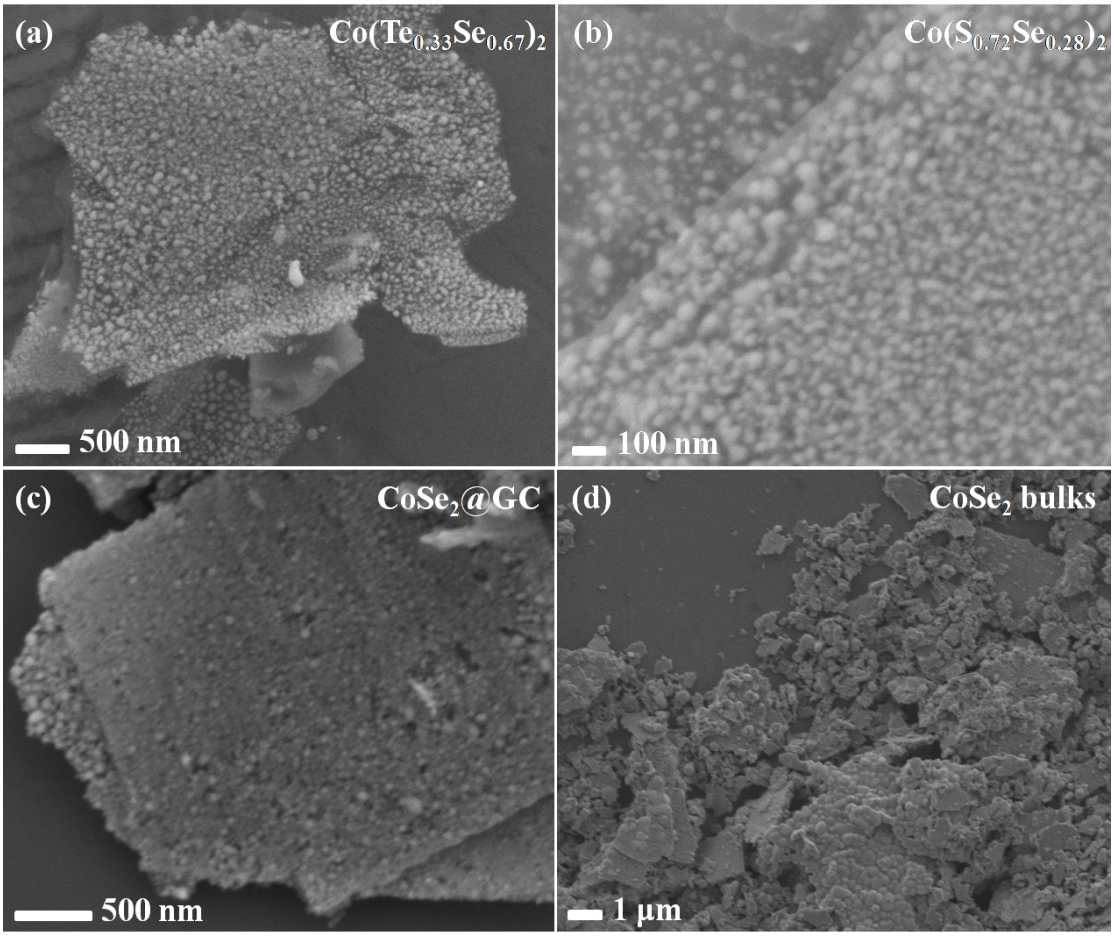

Figure S14. The SEM images of (a) sandwich-like $Co(Te_{0.33}Se_{0.67})_2$, (b) $Co(S_{0.72}Se_{0.28})_2$, (c) $CoSe_2$@GC and (d) $CoSe_2$ bulks after HER measurements.

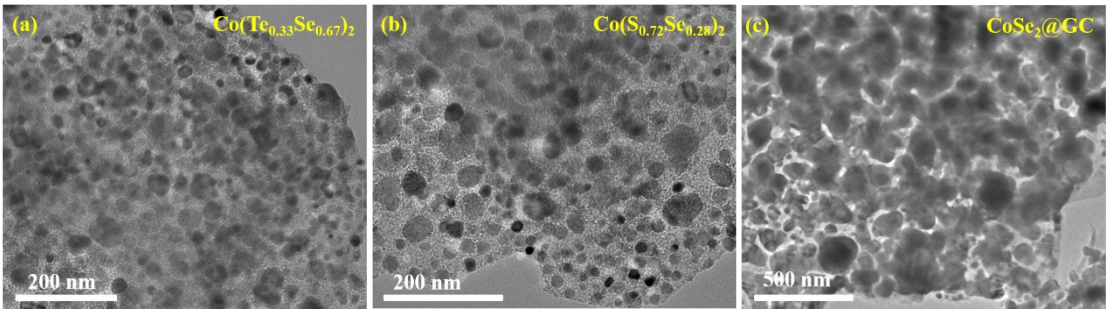

Figure S15. The TEM images of (a) sandwich-like $Co(Te_{0.33}Se_{0.67})_2$, (b) $Co(S_{0.72}Se_{0.28})_2$ and (c) $CoSe_2$@GC after HER measurements.

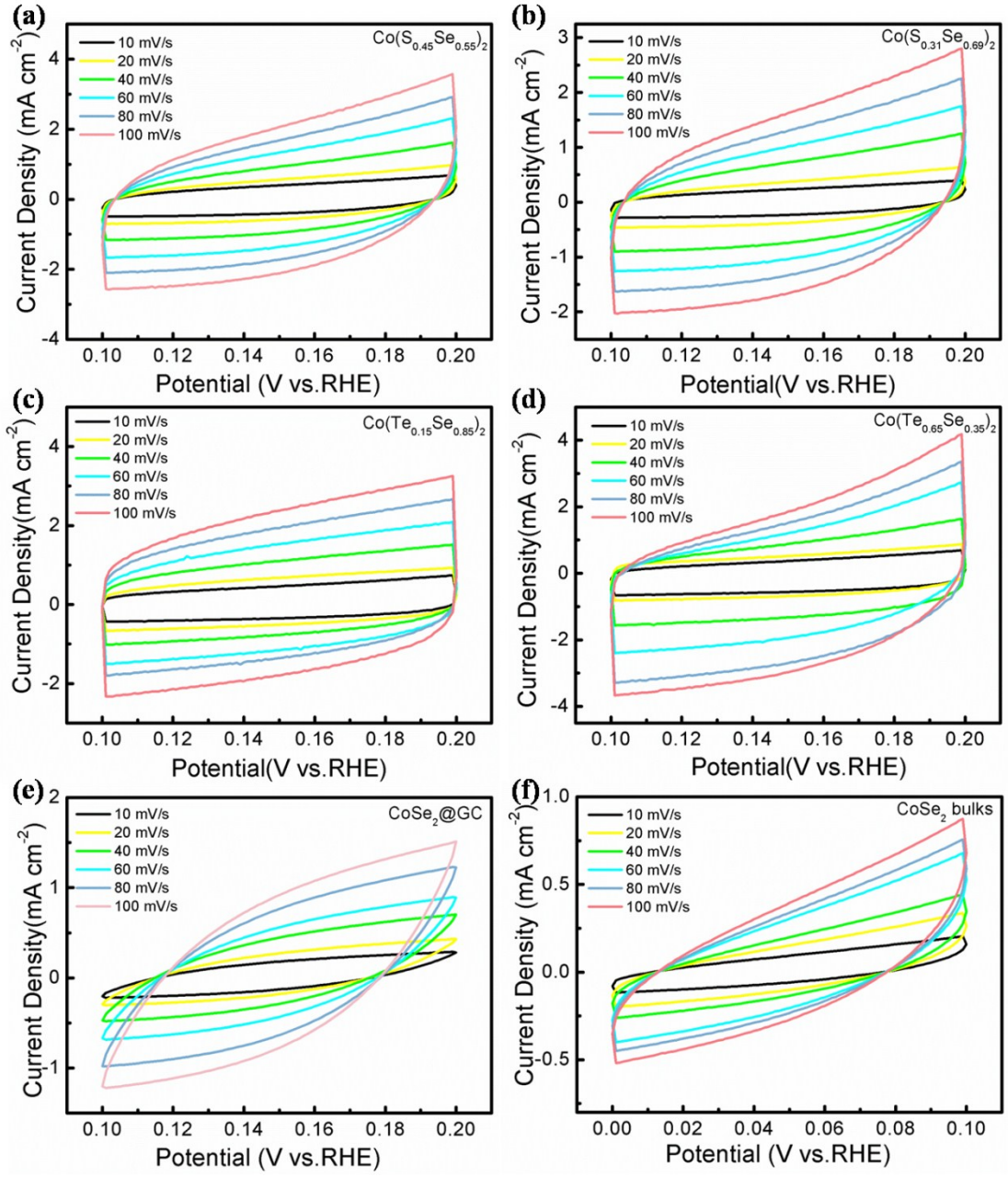

Figure S16. The CV curves in the region of 0.1-0.2 V at different scan rates form 10-100 mV s^{-1} for (a) sandwich-like $Co(S_{0.45}Se_{0.55})_2$, (b) $Co(S_{0.31}Se_{0.69})_2$, (c) $Co(Te_{0.15}Se_{0.85})_2$, (d) $Co(Te_{0.65}Se_{0.35})_2$, (e) $CoSe_2$@GC and (f) $CoSe_2$ bulks.

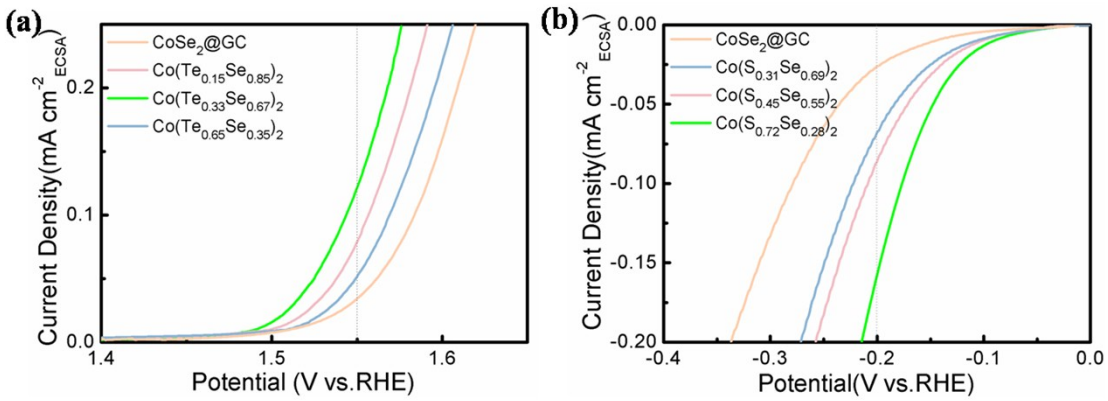

Figure S17. (a) OER polarization curves of sandwich-like $CoSe_2$, $Co(Te_{0.15}Se_{0.85})_2$, $Co(Te_{0.33}Se_{0.67})_2$ and $Co(Te_{0.65}Se_{0.35})_2$ graphitized carbon-based composites, normalized by ECSA. (b) HER polarization curves of sandwich-like $CoSe_2$, $Co(S_{0.31}Se_{0.69})_2$, $Co(S_{0.45}Se_{0.55})_2$ and $Co(S_{0.72}Se_{0.28})_2$ graphitized carbon-based composites, normalized by ECSA.

Table S1. Comparison of OER catalytic performance with other cobalt-based TMDs catalysts on recently available literatures.

Materials	Electrolyte	Onset potential (V)	η_{10} (mV)	Tafel slope (mV dec^{-1})	Reference
Co-P/NC	1 M KOH	1.50	354	52	[22]
$CoSe_2$ nanosheets	0.1 M KOH	-	320	44	[23]
Zn-doped $CoSe_2$	1 M KOH	-	356	88	[19]
NG-$CoSe_2$ nanobelt	0.1 M KOH	1.523	366	-	[24]
CoTe nanotube film	1 M KOH	1.56	370	-	[25]
$CoTe_2$/carbon nanotube	1 M KOH	~1.50	291	44.2	[26]
$CoTe_2$	1 M KOH	~1.53	380	58	[9]
CoSe/Ti mesh	1 M KOH	1.54	292	69	[27]
CoSe nanowalls	1 M KOH	1.59		74.7	[28]
$CoSe_2$ nanocrystals	1 M KOH	1.55	430	50	[29]
CoO_x-CoSe/NF	1 M KOH	1.50	298	68	[30]
Sandwich-like $Co(S_{0.72}Se_{0.28})_2$	1 M KOH	1.52	315	69	This work
Sandwich-like $Co(Te_{0.33}Se_{0.67})_2$	1 M KOH	1.48	272	44	This work

Table S2. Composition of sandwich-like $CoTe_{2x}Se_{2(1-x)}$, $CoS_{2y}Se_{2(1-y)}$, $CoSe_2$@GC, $CoTe_2$@GC and CoS_2@GC, determined by ICP-OES.

$CoTe_{2x}Se_{2(1-x)}$ / $CoS_{2y}Se_{2(1-y)}$	Co (At.%):	S (At.%):	Se (At.%):	Te (At.%)
$CoSe_2$@GC (x=0)	1.01 :	-	1.99 :	-
$Co(Te_{0.15}Se_{0.85})_2$ (x=0.15)	0.98 :	-	1.71 :	0.31
$Co(Te_{0.33}Se_{0.67})_2$ (x=0.33)	1.01 :	-	1.34 :	0.66
$Co(Te_{0.65}Se_{0.35})_2$ (x=0.65)	1.00 :	-	0.69 :	1.31
$CoTe_2$@GC (x=1)	0.99 :	-	-	2.01
$Co(S_{0.31}Se_{0.69})_2$ (y=0.31)	1.02 :	0.62 :	1.37 :	-
$Co(S_{0.45}Se_{0.55})_2$ (y=0.45)	1.01 :	0.91 :	1.10 :	-
$Co(S_{0.72}Se_{0.28})_2$ (y=0.72)	1.01 :	1.43 :	0.56 :	-
CoS_2@GC (y=1)	0.99 :	2.01 :	-	-

Table S3. Resistance values of sandwich-like $Co(Te_{0.33}Se_{0.67})_2$, $Co(S_{0.72}Se_{0.28})_2$, $CoSe_2$@GC and $CoSe_2$ bulks before and after OER measurements.

	$Co(S_{0.72}Se_{0.28})_2$ Ω	$Co(Te_{0.33}Se_{0.67})_2$ Ω	$CoSe_2$@GC Ω	$CoSe_2$ bulks Ω
R_{ct} before OER tests	0.43	0.32	0.96	2.02
R_{ct} after OER tests	1.33	0.58	2.38	4.92

Table S4. Comparison of HER catalytic performance with other non-noble metal catalysts on recently available literatures.

Materials	Electrolyte	Onset overpotential (mV)	η_{10} (mV)	Tafel slope (mV dec^{-1})	Reference
nanofiber@CoS_2 core/sheath	1 M KOH	~150	207	113.3	[31]
$CoTe_2$ nanostrcture	0.5M H_2SO_4		309	-	[32]
CoSe/Ti mesh	1 M KOH	~150	121	84	[33]
Co-P/NC	1 M KOH	~100	191	-	[22]
NiSe-NiO_x/NF	1 M KOH	~150	160	-	[34]
CoO_x-CoSe/NF	1 M KOH	~200	-	94	[30]
$CoP_{2x}Se_{2(1-x)}$ NWs	1 M KOH	~115	120	-	[35]
$MoS_{2(1-x)}Se_{2x}$ nanoflakes	0.5M H_2SO_4	110	~170	-	[10]
$CoSe_2$ microcages	0.5M H_2SO_4	140		95	[36]
NiS/Ni	1 M KOH	-	158	83	[37]
$CoS_{2x}Se_{2(1-x)}$ nanowire array	0.5M H_2SO_4	~120	129.5	-	[21]
Sandwich-like $Co(S_{0.72}Se_{0.28})_2$	1 M KOH	62	106	80	This work
Sandwich-like $Co(Te_{0.33}Se_{0.67})_2$	1 M KOH	131	199	117	This work

Table S5. The values of ΔE(H^*), ZPE(H^*), ΔZPE and ΔG(H^*) of the H^* at the different adsorption sites on the surface of different models.

Models	Adsorption sites	ΔE(H^*)/eV	ZPE(H^*)/eV	ΔZPE/eV	ΔG(H^*)/eV
$CoSe_2$	Co	-0.820	0.184	0.037	-0.583
	Se	-1.320	0.184	0.037	-1.083
$Co(S_{0.31}Se_{0.69})_2$	Co	-0.570	0.188	0.041	-0.329
	Se	0.189	0.194	0.047	0.436
$Co(S_{0.45}Se_{0.55})_2$	Co	-0.450	0.184	0.037	-0.213
	Se	-0.570	0.208	0.061	-0.309
$Co(S_{0.72}Se_{0.28})_2$	Co	-0.040	0.170	0.023	0.183
	Se	0.059	0168	0.021	0.280
CoS_2	Co	-0.900	0.179	0.032	-0.668
	S	-0.950	0.185	0.038	-0.712

Table S6. Resistance values of sandwich-like $Co(Te_{0.33}Se_{0.67})_2$, $Co(S_{0.72}Se_{0.28})_2$, $CoSe_2$@GC and $CoSe_2$ bulks before and after HER measurements.

	$Co(S_{0.72}Se_{0.28})_2$ Ω	$Co(Te_{0.33}Se_{0.67})_2$ Ω	$CoSe_2$@GC Ω	$CoSe_2$ bulks Ω
R_{ct} before HER tests	1.54	4.01	12.40	29.13
R_{ct} after HER tests	2.15	6.97	21.13	42.10

Table S7. Comparison of C_{dl}, ECSA, R_f, j_{geo} and j_{ECSA} of OER in 1M KOH.

Catalysts	C_{dl} (mF cm^{-2})	ECSA (mF cm^{-2})	R_f	$j_{\eta=320\,mV,\ ECSA}$ (mA cm^{-2})
$CoSe_2$@GC	8.1	16.2	202.5	0.035
$Co(Te_{0.15}Se_{0.85})_2$	21.1	42.2	527.5	0.121
$Co(Te_{0.33}Se_{0.67})_2$	24.7	49.4	617.5	0.080
$Co(Te_{0.65}Se_{0.35})_2$	16.6	33.2	415.0	0.052

As reported in literature (*Nat. Commun.* **2016,** *7*, 11981-11989), twice C_{dl} represents the corresponding electrochemical active surface area (ECSA). Therefore, ECSA could be obtained according to the value of C_{dl}. Additionally, the specific capacitance (C_s) for an ideal flat surface is generally found to be in the range of 20-60 μF cm^{-2}, and it is assumed as 40 μF cm^{-2} in the following calculations of roughness factor (R_f). And R_f is calculated via dividing C_{dl} by the C_s (40 μF cm^{-2}). Then, the specific OER activity is determined via normalizing the current density by the corresponding ECSA, according to the R_f.

Table S8. Comparison of C_{dl}, ECSA, R_f, j_{geo} and j_{ECSA} of HER in 1M KOH.

Catalysts	C_{dl} (mF cm^{-2})	ECSA (mF cm^{-2})	R_f	$j_{\eta=200\,mV,\ ECSA}$ (mA cm^{-2})
$CoSe_2$@GC	8.1	16.2	202.5	-0.026
$Co(S_{0.31}Se_{0.69})_2$	15.5	31.0	387.5	-0.068
$Co(S_{0.45}Se_{0.55})_2$	18.6	37.2	465.0	-0.086
$Co(S_{0.72}Se_{0.28})_2$	23.2	46.4	580.0	-0.158

Table S9. Performance comparison of overall water splitting with other systems in alkaline electrolyte.

Materials	Electrolyte	Potential/current density	stability	Reference
Pt/C || IrO_2	1 M KOH	1.52 V/10 mA cm^{-2}	16 h	[38]
$Co_{0.13}Ni_{0.87}Se_2$ || $Co_{0.13}Ni_{0.87}Se_2$	1 M KOH	1.63 V/10 mA cm^{-2}	10 h	[39]
$NiCo_2S_4$ || $NiCo_2S_4$	1M KOH	1.68 V/10 mA cm^{-2}	10 h	[40]
Ni_3Se_2/CF || Ni_3Se_2/CF	1 M KOH	1.65 V/10 mA cm^{-2}	12 h	[41]
CoSe/Ti||CoSe/Ti	1 M KOH	1.65 V/10 mA cm^{-2}	27 h	[27]
CoSe||CoSe	1 M KOH	~1.75 V/10 mA cm^{-2}	24 h	[28]
NiSe-NiO_x/NF	1 M KOH	1.68 V/10 mA cm^{-2}	40 h	[34]
CoO_x-CoSe/NF||CoO_x-CoSe/NF	1 M KOH	1.66 V/10 mA cm^{-2}	40 h	[30]
NiS/Ni foam||NiS/Ni foam	1 M KOH	1.64 V/10 mA cm^{-2}	35 h	[37]
$Co(S_{0.72}Se_{0.28})_2$||$Co(Te_{0.33}Se_{0.67})_2$	1 M KOH	1.62V/10 mA cm^{-2}	40 h	This work

Table S10. Details of the reaction conditions for the sandwich-like $CoTe_{2x}Se_{2(1-x)}$ and $CoS_{2y}Se_{2(1-y)}$ composites.

Samples	sandwich-like Co nanoparticles	S powders	Se powders	Te powders	Calcinations temperature
$CoSe_2$@GC	100 mg	-	1000 mg	-	540 °C
$Co(Te_{0.15}Se_{0.85})_2$	100 mg	-	850 mg	150 mg	700 °C
$Co(Te_{0.33}Se_{0.67})_2$	100 mg	-	600 mg	400 mg	700 °C
$Co(Te_{0.65}Se_{0.35})_2$	100 mg	-	200 mg	800 mg	700 °C
$CoTe_2$@GC	100 mg	-	-	1000 mg	720 °C
$Co(S_{0.31}Se_{0.69})_2$	100 mg	200 mg	800 mg	-	540 °C
$Co(S_{0.45}Se_{0.55})_2$	100 mg	300 mg	700 mg	-	540 °C
$Co(S_{0.72}Se_{0.28})_2$	100 mg	600 mg	400 mg	-	540 °C
CoS_2@GC	100 mg	1000 mg	-	-	540 °C

Notes and Reference

1. J. P. Perdew, K. Burke and M. Ernzerhof, *Phys. Rev. Lett.*, 1996, **77**, 3865-3868.
2. G. Kresse and D. Joubert, *Phys Rev B*, 1999, **59**, 1758-1775.
3. X. Gu, J. L. Liu, J. H. Yang, H. J. Xiang, X. G. Gong and Y. Y. Xia, *J. Phys. Chem. C*, 2011, **115**, 12672-12676.
4. L. Fang, Z. Q. Jiang, H. T. Xu, L. Liu, Y. X. Guan, X. Gu and Y. Wang, *J. Catal.*, 2018, **357**, 238-246.
5. L. L. Feng, G. T. Yu, Y. Y. Wu, G. D. Li, H. Li, Y. H. Sun, T. Asefa, W. Chen and X. X. Zou, *J. Am. Chem. Soc.*, 2015, **137**, 14023-14026.
6. J. K. Norskov, T. Bligaard, A. Logadottir, J. R. Kitchin, J. G. Chen, S. Pandelov and J. K. Norskov, *J. Electrochem. Soc.*, 2005, **152**, J23-J26.
7. K. N. Kudin, B. Ozbas, H. C. Schniepp, R. K. Prud'homme, I. A. Aksay and R. Car, *Nano Lett.*, 2008, **8**, 36-41.
8. Y. W. Liu, X. M. Hua, C. Xiao, T. F. Zhou, P. C. Huang, Z. P. Guo, B. C. Pan and Y. Xie, *J. Am. Chem. Soc.*, 2016, **138**, 5087-5092.
9. I. G. McKendry, A. C. Thenuwara, J. W. Sun, H. W. Peng, J. P. Perdew, D. R. Strongin and M. J. Zdilla, *ACS Catal.*, 2016, **6**, 7393-7397.
10. Q. F. Gong, L. Cheng, C. H. Liu, M. Zhang, Q. L. Feng, H. L. Ye, M. Zeng, L. M. Xie, Z. Liu and Y. G. Li, *ACS Catal.*, 2015, **5**, 2213-2219.
11. H. L. Li, X. D. Duan, X. P. Wu, X. J. Zhuang, H. Zhou, Q. L. Zhang, X. L. Zhu, W. Hu, P. Y. Ren, P. F. Guo, L. Ma, X. P. Fan, X. X. Wang, J. Y. Xu, A. L. Pan and X. F. Duan, *J. Am. Chem. Soc.*, 2014, **136**, 3756-3759.
12. C. B. Ouyang, X. Wang and S. Y. Wang, *Chem. Commun.*, 2015, **51**, 14160-14163.
13. B. F. Cao, G. M. Veith, J. C. Neuefeind, R. R. Adzic and P. G. Khalifah, *J. Am. Chem. Soc.*, 2013, **135**, 19186-19192.
14. Z. C. Xing, Q. Liu, A. M. Asiri and X. P. Sun, *Adv. Mater.*, 2014, **26**, 5702-5707.
15. D. S. Kong, H. T. Wang, Z. Y. Lu and Y. Cui, *J. Am. Chem. Soc.*, 2014, **136**, 4897-4900.
16. C. P. Lee, W. F. Chen, T. Billo, Y. G. Lin, F. Y. Fu, S. Samireddi, C. H. Lee, J. S. Hwang, K. H. Chen and L. C. Chen, *J. Mater. Chem. A*, 2016, **4**, 4553-4561.
17. H. Vanderheide, R. Hemmel and C. F. Vanbruggen, *J. Solid State Chem.*, 1980, **33**, 17-25.
18. K. Adachi, M. Matsui and Y. Omata, *J. Phys. Soc. Jpn*, 1981, **50**, 83-89.
19. Q. C. Dong, Q. Wang, Z. Y. Dai, H. J. Qiu and X. C. Dong, *ACS Appl. Mater. Interfaces*, 2016, **8**, 26902-26907.
20. M. S. Khan, M. N. Ashiq, M. F. Ehsan, T. He and S. Ijaz, *Appl. Catal., A*, 2014, **487**, 202-209.
21. K. L. Liu, F. M. Wang, K. Xu, T. A. Shifa, Z. Z. Cheng, X. Y. Zhan and J. He, *Nanoscale*, 2016, **8**, 4699-4704.
22. B. You, N. Jiang, M. L. Sheng, S. Gul, J. Yano and Y. J. Sun, *Chem. Mater.*, 2015, **27**, 7636-7642.
23. Y. W. Liu, H. Cheng, M. J. Lyu, S. J. Fan, Q. H. Liu, W. S. Zhang, Y. D. Zhi, C. M. Wang, C. Xiao, S. Q. Wei, B. J. Ye and Y. Xie, *J. Am. Chem. Soc.*, 2014, **136**, 15670-15675.
24. M. R. Gao, X. Cao, Q. Gao, Y. F. Xu, Y. R. Zheng, J. Jiang and S. H. Yu, *Acs Nano*, 2014, **8**, 3970-3978.

25. S. A. Patil, E. K. Kim, N. K. Shrestha, J. Chang, J. K. Lee and S. H. Han, *ACS Appl. Mater. Interfaces*, 2015, **7**, 25914-25922.
26. T. H. Lu, C. J. Chen, Y. R. Lu, C. L. Dong and R. S. Liu, *J. Phys. Chem. C*, 2016, **120**, 28093-28099.
27. T. T. Liu, Q. Liu, A. M. Asiri, Y. L. Luo and X. P. Sun, *Chem. Commun.*, 2015, **51**, 16683-16686.
28. X. Li, L. Zhang, M. R. Huang, S. Y. Wang, X. M. Li and H. W. Zhu, *J. Mater. Chem. A*, 2016, **4**, 14789-14795.
29. I. H. Kwak, H. S. Im, D. M. Jang, Y. W. Kim, K. Park, Y. R. Lim, E. H. Cha and J. Park, *ACS Appl. Mater. Interfaces*, 2016, **8**, 5327-5334.
30. X. J. Xu, P. Y. Du, Z. K. Chen and M. H. Huang, *J Mater. Chem. A*, 2016, **4**, 10933-10939.
31. H. H. Gu, Y. P. Huang, L. Z. Zuo, W. Fan and T. X. Liu, *Inorg. Chem. Front.*, 2016, **3**, 1280-1288.
32. K. Wang, Z. G. Ye, C. Q. Liu, D. Xi, C. J. Zhou, Z. Q. Shi, H. Y. Xia, G. W. Liu and G. J. Qiao, *ACS Appl. Mater. Interfaces*, 2016, **8**, 2910-2916.
33. T. T. Liu, Q. Liu, A. M. Asiri, Y. L. Luo and X. P. Sun, *Chem. Commun.*, 2015, **51**, 16683-16686.
34. R. Q. Gao, G. D. Li, J. B. Hu, Y. Y. Wu, X. R. Lian, D. J. Wang and X. X. Zou, *Catal. Sci. Technol.*, 2016, **6**, 8268-8275.
35. K. L. Liu, F. M. Wang, T. A. Shifa, Z. X. Wang, K. Xu, Y. Zhang, Z. Z. Cheng, X. Y. Zhan and J. He, *Nanoscale*, 2017, **9**, 3995-4001.
36. C. H. Mu, H. X. Qi, Y. Q. Song, Z. P. Liu, L. X. Ji, J. G. Deng, Y. B. Liao and F. Scarpa, *RSC Adv.*, 2016, **6**, 23-30.
37. W. X. Zhu, X. Y. Yue, W. T. Zhang, S. X. Yu, Y. H. Zhang, J. Wang and J. L. Wang, *Chem. Commun.*, 2016, **52**, 1486-1489.
38. X. B. Yu, S. Zhang, C. Y. Li, C. L. Zhu, Y. J. Chen, P. Gao, L. H. Qi and X. T. Zhang, *Nanoscale*, 2016, **8**, 10902-10907.
39. T. T. Liu, A. M. Asiri and X. P. Sun, *Nanoscale*, 2016, **8**, 3911-3915.
40. D. N. Liu, Q. Lu, Y. L. Luo, X. P. Sun and A. M. Asiri, *Nanoscale*, 2015, **7**, 15122-15126.
41. J. L. Shi, J. M. Hu, Y. L. Luo, X. P. Sun and A. M. Asiri, *Catal. Sci. Technol.*, 2015, **5**, 4954-4958.